Oxygen deficiency induced strong electron localization in lanthanum doped transparent perovskite oxide BaSnO$_3$

Jiameng Cui,[1,*] Yingying Zhang,[1,*] Jianlin Wang ⓞ,[2,3,†] Zhibo Zhao,[1] Haoliang Huang,[2] Wei Zou,[1] Mengmeng Yang,[4] Ranran Peng,[1,4] Wensheng Yan,[2] Qiuping Huang,[4] Zhengping Fu,[1,4,‡] and Yalin Lu[1,2,3,4,§]

[1]*Department of Materials Science and Engineering, University of Science and Technology of China, Hefei 230026, People's Republic of China*
[2]*National Synchrotron Radiation Laboratory, University of Science and Technology of China, Hefei 230026, People's Republic of China*
[3]*Synergetic Innovation Center of Quantum Information & Quantum Physics, University of Science and Technology of China, Hefei 230026, People's Republic of China*
[4]*Hefei National Laboratory for Physical Sciences at the Microscale, University of Science and Technology of China, Hefei 230026, People's Republic of China*

In this paper, we prepare heavily electron doped La$_{0.04}$Ba$_{0.96}$SnO$_3$ (LBSO) thin films on a SrTiO$_3$ (STO) substrate by the pulsed laser deposition method under different oxygen pressures, in which different levels of oxygen vacancy concentrations are present. Normally, oxygen vacancies are implicitly assumed as isolated point defects that dope the materials with electron carriers, whereas oxygen-deficient LBSO films exhibit an apparent metal-to-insulator transition combined with lower carrier concentrations and mobility with increased oxygen vacancies, which are concluded from the transport measurement data. Considering the almost constant density of threading dislocations and the higher formation energies for other intrinsic crystal defects, the observed transport trends are ascribed to the extra oxygen vacancies introduced. Therefore, strong electron localization originating from the interaction between the oxygen vacancy and La impurity is proposed for interpreting the behavior in oxygen-deficient LBSO films. Oxygen-deficient crystal structure models for LBSO have been optimized and the electronic structures are revealed by first-principles calculations based on the density functional theory. The partial density of states results indicate that strong electron localization comes from the deep strongly localized states in the forbidden gap, which are mainly composed of hybridized orbitals of O $2p$ with Sn $5s5p$ and some amount of Sn $4d$. Thus, the control of the oxygen defects and the related electronic states in barium stannate is essential for achieving optimal electrical performance and as potential applications in perovskite heterostructure devices.

I. INTRODUCTION

Barium stannate (BaSnO$_3$) with an ideal cubic perovskite structure, which behaves as a wide band-gap semiconductor and has a high-temperature stability up to 1000 °C [1], has been proposed as an alternative transparent conducting oxide (TCO) material for the well-known Sn doped In$_2$O$_3$ (ITO) [2]. Analogous to the local density approximation (LDA) result of ITO, the spatially delocalized conduction band of BaSnO$_3$ mainly consists of metallic Sn $5s$ orbitals, is highly dispersive with an optical gap larger than 3 eV from the valence band maximum, and predicts a low electron effective mass m^* of $0.2m_0$ [3,4]. It indicates the potential for good electrical mobility coupled with high optical transmission. Compared with conventional binary oxides, doped BaSnO$_3$ with a ternary perovskite structure is more flexible in structural modification and the controllability of properties. An unusually high mobility μ that was reached 320 cm^2 V^{-1} s^{-1} at room temperature (RT) was reported in La doped BaSnO$_3$ single crystals [5,6], which was the highest value among the known TCO materials. For La$_x$Ba$_{1-x}$SnO$_3$/BaSnO$_3$ thin films epitaxially grown on (001) SrTiO$_3$, the record of μ is only up to 120 cm^2 V^{-1} s^{-1}, which is mainly ascribed to the extra misfit/threading dislocations induced by the lattice mismatch [7]. Additionally, perovskite-type oxides have displayed their impressive multifunctionality such as colossal magnetoresistance [8], superconductivity [9], ferroelectric polarization [10], and multiferroicity [11]. It is appealing to develop other perovskite TCOs that may be valuable for practical applications and thus to realize transparent all-perovskite electronic devices with unexpected quantum physical properties.

In addition to impurity doping, the oxygen vacancy is a fundamental and intrinsic nonstoichiometric defect in perovskite oxides. The subtle deviation of oxygen occupancy from ideal stoichiometry plays a crucial role in the evolution of their physical properties, such as superconductivity [12], and electrical [13] and magnetic properties [14]. In many cases, the degradations or failures of perovskite oxide devices also resulted from changes in the oxygen defects [15,16]. Moreover, self-doping of the oxygen vacancy is easily realized via various processes of growth and post-treatment, such as low oxygen pressure [17,18], reducing conditions [19], or

---

*These authors contributed equally to this work.
†Corresponding author: wangjl@ustc.edu.cn
‡fuzp@ustc.edu.cn
§yllu@ustc.edu.cn

postannealing [20,21]. Thus, the cubic perovskite $BaSnO_3$ is versatile enough to modify and extend their properties by inducing charged point defects, such as oxygen vacancies and doped impurities. A systematic understanding of how charged point defects influence electronic transport is fundamental for further insights into perovskite oxide-based devices. It is worth grasping the electronic mechanisms that enable us to optimize and control the properties of the highly doped $BaSnO_3$ with abundant defects, which is essential for realizing the desired thin film, interface, and surface in different functional devices.

It is generally recognized that oxygen vacancies act as electron donors in oxygen-deficient $BaSnO_3$ and provide electron carriers [17–21] in oxides. Therefore, dramatic changes in the transport behaviors are anticipated. The charged point defects in the oxygen-deficient $BaSnO_3$ system with heavy chemical impurity doping play a key role in the mobility-limited scattering processes on the transport property. In this paper, we have carried out systematic experiments on oxygen-deficient $La_{0.04}Ba_{0.96}SnO_3$ (LBSO) thin films epitaxially grown on (001) $SrTiO_3$ substrates by pulsed laser deposition (PLD) combined with theoretical analyses by density functional theory (DFT) calculations. Contrary to the typical behaviors of the reported oxygen-deficient $BaSnO_3$ with a resistivity that was varied from the insulating to metallic by the introduced oxygen vacancies [17,18,21], our oxygen-deficient $BaSnO_3$ with an extra heavy La impurity experiences an opposite transition from a metallic state to an insulating state, followed by a decrease in carrier concentration and mobility. We attribute these contrary results to the defect-defect interactions between the oxygen vacancies and La dopants in the oxygen-deficient LBSO material system, which are accompanied by deep localized states in the forbidden gap and their associated strong electron localization.

II. EXPERIMENT

A stoichiometric $La_{0.04}Ba_{0.96}SnO_3$ ceramic target was prepared by the traditional solid-state method. Epitaxial LBSO films were prepared on (001) $SrTiO_3$ single-crystal substrates by PLD (Pascal Company, Ltd., Japan) with a KrF excimer laser ($\lambda = 248$ nm). The pulse energy and frequency irradiated on the target were maintained at 120 mJ and 2 Hz. During the film synthesis, the substrate temperature was kept at 850 °C and the growth oxygen pressures varied from 1 to 20 Pa. After deposition, the samples were *in situ* annealed for 30 min at 100 Pa with a lower temperature (800 °C) and then cooled down to room temperature with a cooling rate of 20 °C/min. The structural analyses were conducted on the Rigaku SmartLab high-resolution x-ray diffraction [XRD, Cu $K\alpha$ radiation, Ge(220) two-bounce monochromators]. The temperature-dependent electrical characteristics of the samples were measured using a physical property measurement system (PPMS, Quantum Design, USA). The transmission electron microscopy (TEM) characterizations were conducted with a JEM-ARM200F system to get the bright-field images on the cross section. X-ray absorption spectroscopy (XAS) measurements were performed on the BL12B-a beamline at the National Synchrotron Radiation Laboratory (Hefei, China) to investigate the electronic

structure of LBSO thin films. X-ray photoelectron spectroscopy (XPS) with a monochromatized Mg $K\alpha$ x-ray source was used to compare the relative oxygen vacancy concentrations of the films.

First-principles DFT calculations were performed based on the LDA scheme to examine the role of defect-defect interactions on the electronic structures in the oxygen vacancy and La impurity doped $BaSnO_3$. All the calculations were done by using the Vienna *ab initio* simulation package (VASP) within the density functional approximation [22]. A kinetic energy cutoff of 400 eV was used in the plane-wave basis set. The Brillouin zone (BZ) was sampled with a $2 \times 2 \times 2$ special k-point grid. For determining the relative stability of different doping sites, defects were calculated in a $3 \times 3 \times 3$ supercell based on the cubic $Pm3m$ perovskite structure of $BaSnO_3$. After the calculations, all atomic coordinates were relaxed, and the Hellmann-Feynman force reached less than 0.02 eV/Å.

III. RESULTS AND DISCUSSION

A. XRD characterizations for the films prepared under different oxygen pressures

High-quality epitaxial LBSO thin films can be prepared in a wide range of oxygen pressures, from 1 to 15 Pa, as shown in Fig. 1(a). The XRD patterns (θ-2θ scans) of the as-grown films show only the (00*l*) Bragg reflections, suggesting heteroepitaxial LBSO structures oriented normal to the (001) STO substrate surface without secondary phases. The (002) LBSO reflection peaks shift gradually to the lower 2θ angle and the corresponding c-axis lattice parameters derived from the reflection peaks of the films prepared under a series of oxygen pressures are plotted in Fig. 1(b). For samples grown under oxygen pressures that varied from 7.5 to 15 Pa, the c-axis parameters, around 4.117–4.120 Å, are very close and comparable to that of LBSO ($a_c = 4.118$ Å). With a further oxygen-deficient environment, the lattices undergo a monotonic increasing toward 4.171 Å (grown with 1 Pa). When the films are grown under a lower oxygen pressure, more oxygen vacancies are expected, which is confirmed by the XPS results discussed below. We anticipate that the lattice will experience an expansion, as a result of the enhanced Coulomb repulsion originating from the increasing concentration of charged defects (V_O) [17]. Increased lattice constants with a reduced oxygen pressure have also been reported in other oxygen-deficient perovskites [17,18]. Considering the lattice constants of the thin film and the substrate, the lattice mismatch between LBSO ($a_c = 4.118$ Å) and STO ($a_c = 3.905$ Å) is about 5.45%. Such a large lattice mismatch develops grain boundaries and dislocations in the epitaxial LBSO films. Although disorders were introduced by the large lattice mismatch, all films were still highly crystallized as the narrow full width at half maximum (FWHM) in the rocking curves of (002) LBSO peaks. Both the high crystallinity and phase purity of the perovskite structure are available within a broad oxygen pressure range. The (002) film peaks widened slightly with increasing oxygen pressure up to 15 Pa, meanwhile further worsening of the crystalline quality should be noticed under the higher oxygen atmosphere. A (002) FWHM of 2.278°
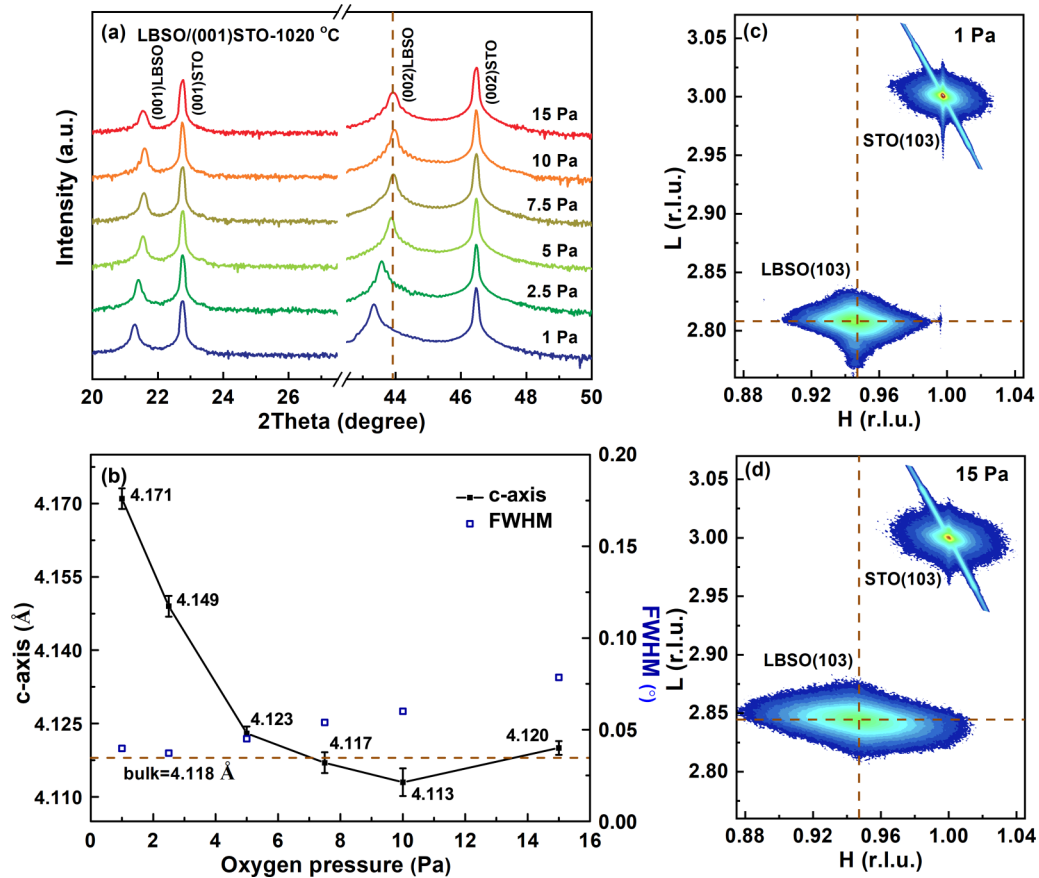
FIG. 1. (a) The XRD θ-2θ scans of LBSO/(001)STO heterostructures deposited at six different oxygen pressures of 15, 10, 7.5, 5, 2.5, and 1 Pa, respectively. (b) Out-of-plane lattice parameters and the corresponding full width at half maximum (FWHM) of (002) LBSO diffraction peaks as a function of growth oxygen pressures. RSM around the (103) STO and the (103) LBSO reflections at (c) 1 Pa and (d) 15 Pa, respectively.

from the sample grown under 20 Pa was obtained (see the Supplemental Material [23] for additional XRD results in Fig. S1, which also includes Refs. [24–36]).

XRD reciprocal space mappings (RSMs) were conducted to investigate the strain state in LBSO films. Figures 1(c) and 1(d) show asymmetrical RSMs around the (103) reflections of STO and LBSO thin films grown at 1 and 15 Pa, respectively. The (103) LBSO reflection dots of the films grown at 1 Pa have higher peak intensities and narrower widths than those grown under higher oxygen conditions, suggesting a better crystal quality, which is consistent with the results of XRD scans mentioned above. The in-plane lattice parameters are calculated to be about 4.120 Å at 1 Pa and 4.124 Å at 15 Pa. The RSM data for the rest of samples are shown in Fig. S2 of the Supplemental Material [23]. All oxygen pressure variable samples show similar in-plane lattice parameters. Therefore, the epitaxial strain of all LBSO layers is almost completely relaxed, which is attributed to the large lattice mismatch with the STO substrates. It can be noted that there is an expansion of the c-axis lattice with decreasing deposition oxygen pressure, meanwhile the a/b-axis lattice is nearly unchanged, suggesting the effects of substrate constraint. The ratio of the c axis over the a/b axis varies from 0.999 to 1.013 as the variation of the resulting structures.

B. Oxygen deficiency confirmed by XPS measurements

To quantify the relative oxygen-related defect concentrations in these La doped BaSnO$_3$ films of variable growth oxygen pressures, we have performed O $1s$ core-level XPS spectra as shown in Fig. 2. The spectra can be deconvoluted into three different contributions: The low-energy component (528.8 eV) originates from the oxygen in oxide lattices, the middle peak (530.8 eV) corresponds to the oxygen within the nonstoichiometric La doped BaSnO$_{3-\delta}$ of the oxygen-deficient regions, and the one at the high-energy component (533.6 eV) which is only observed in the films of 1 Pa in our experiments belongs to the loosely bound oxygen or hydroxyl species on the film surface [18,37]. Therefore, changes in the integrated area ratios of the oxygen-deficient component (including the peaks at 530.8 and 533.6 eV) to the lattice oxygen component may be connected to the relative variations in the concentration of oxygen vacancies. In Table I, we list the O$_{nonlattice}$/O$_{lattice}$ ratios of the samples grown under different oxygen pressures. It is noteworthy that the highest oxygen vacancy concentration appears at the lowest deposition oxygen pressure. Nonstoichiometric oxygen vacancies decrease with increasing growth oxygen pressure until it reaches a minimum at a pressure of 7.5 Pa. A slight increase
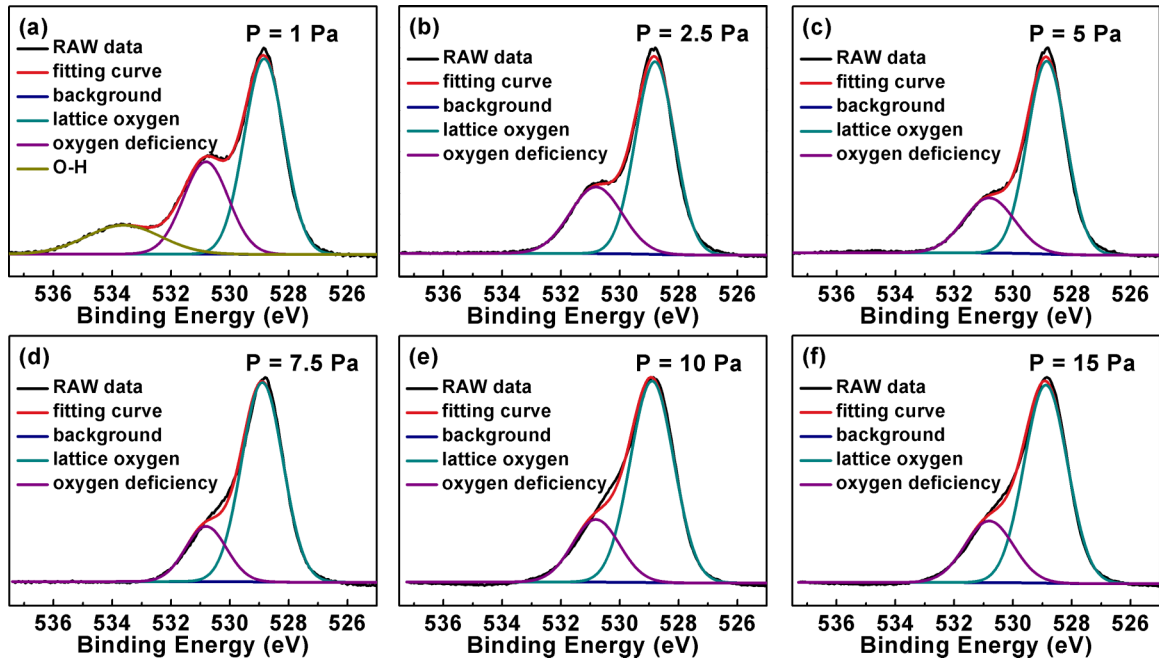
FIG. 2. XPS O 1s spectra of La doped BaSnO$_3$ thin films deposited on the growth oxygen pressures of (a) 1 Pa, (b) 2.5 Pa, (c) 5 Pa, (d) 7.5 Pa, (e) 10 Pa, and (f) 15 Pa, respectively. The experimental data were deconvoluted into three components at about 528.8, 530.8, and 533.6 eV.

in the O$_{nonlattice}$/O$_{lattice}$ ratios at higher oxygen pressures may be attributed to the oxygen deficiency that originates from the lattice disorders due to the deteriorated crystalline quality (referred to the XRD results in Fig. 1). Therefore, this series of XPS spectra confirms that the relative oxygen deficiencies of the films increase during lower oxygen deposition conditions.

C. Electrical transport properties

A subtle modification of the oxygen vacancy concentration significantly influences the evolution of electrical transports. Detailed analyses of the electrical transport properties (resistivity ρ, carrier concentration n, and mobility μ) of these V_O-variable LBSO thin films are obtained as functions of temperature. The schematic illustration of the films and the Au electrodes used for measurements is shown in the inset of Fig. S3 of the Supplemental Material [23]. According to the ρ-T characteristics from Fig. 3(a), the T dependence of ρ changes dramatically for the samples with slightly different deposition oxygen pressures. The RT resistivity increases monotonically with decreasing deposition oxygen pressures (increasing oxygen vacancies). A 10^2-fold increase in $\rho(300 \text{ K})$ for samples from 7.5 to 1 Pa, and an obvious transition crossing from metallic to insulating behavior occur. For films grown on 7.5 Pa, a dominant metalliclike behavior can be observed down to 20 K, while resistivity begins to

TABLE I. The O$_{nonlattice}$/O$_{lattice}$ ratios as a function of oxygen pressures from 1 to 15 Pa.

Oxygen pressure (Pa)	1	2.5	5	7.5	10	15
O$_{nonlattice}$/O$_{lattice}$		0.8129	0.4604	0.3703	0.2741	0.3344	0.3473

increase at lower temperatures when donors begin to freeze out. A rapid increase of the metal-insulator transition temperature (T_M) followed by the complete characteristic of semiconducting behavior for the 1-Pa sample is revealed in the data for higher oxygen vacancy concentrations, accompanying an overall rise of ρ in the measured temperature range.

A series of conductive models have been applied to the ρ-T data to get a better understanding of the transport properties. Good linear relationships between ρ and $-\ln T$, as displayed in Figs. S3(a)–S3(d) (see Fig. S3 in the Supplemental Material [23] for a linear fitting of the R-T curves), are observed over the semiconducting regime (below T_M), suggesting that two-dimensional weak localization [38] dominates the conduction mechanism. Similar behaviors have been previously found in La doped BaSnO$_3$ [39] and oxygen-deficient BaSnO$_3$ [17] thin films. Above the T_M temperature, a T^2 dependence of resistivity ($\rho \sim T^2$) is observed, signaling the beginning of the predominance of delocalization effects and electron-electron interactions. The linear fitting relationships between ρ and $-\ln T$ or between ρ and T^2 are also presented in Fig. S3 of the Supplemental Material [23]. This result reveals that electrons become more localized due to oxygen deficiency (reduced oxygen pressures), which is proved by an increase of T_M and concomitant resistivity at the whole measured temperature range.

Carrier concentrations and Hall mobilities measured with a temperature dependence are exhibited for further investigation. As shown in Fig. 4(a), the carrier concentrations are essentially invariant in the temperature range, evidencing a typical trait of degenerate doping with an absent donor activation energy. Considering each La donor provides one free electron, a carrier concentration of 5.72×10^{20} cm^{-3} would be expected in Ba$_{0.96}$La$_{0.04}$SnO$_3$ films. Experimental results reveal that the films with the best conductivity grown in
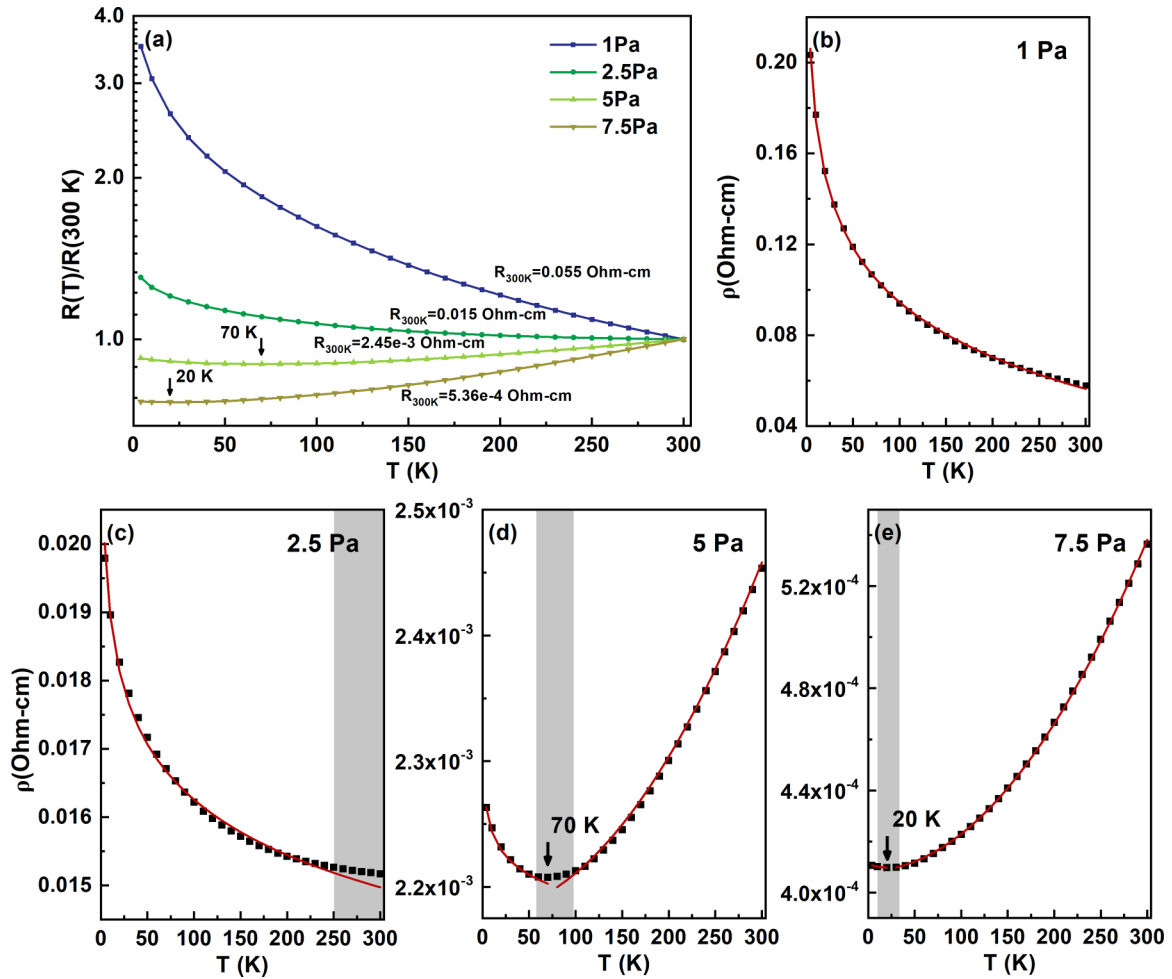
FIG. 3. (a) The normalized resistance-temperature (*R-T*) curves of LBSO films grown under oxygen pressures from 1 to 15 Pa, in which temperatures marked by black arrows represent metal-insulator transition points. Temperature-dependent resistivities were measured for the films grown at (b) 1 Pa, (c) 2.5 Pa, (d) 5 Pa, and (e) 7.5 Pa, respectively. The experimental data are symbolized by black square dots and the red solid lines represent functional dependency fitting with $\rho \propto -\ln T$ and $\rho \propto T^2$, respectively. Gray shapes in (c)–(e) represent the approximate temperature range in which the transition crossing from metallic to insulating behavior occurs.

7.5 Pa have a room-temperature effective carrier concentration of $7.5 \times 10^{20}\,\mathrm{cm}^{-3}$ with an activation ratio slightly exceeding 100%, which can be attributed to the trivially deviated chemical composition of the ceramic target or extra free carriers from oxygen deficiency. Interestingly, we notice that there is a decrease of the carrier concentration followed by a decrease in mobility [Fig. 4(b)] when extra oxygen vacancies are introduced, which is contrary to the previous works for the typical behavior of oxygen-deficient BaSnO$_3$ [17,18,21].

Moreover, the mobilities show different temperature-dependent behaviors depending on the oxygen pressures. Films with a higher oxygen pressure exhibit higher mobilities and a negative temperature coefficient contrary to the lower one. We attribute these mobility-limited scattering processes to the collective effect of the dislocation scattering and the oxygen-vacancy-introduced variation of carrier concentrations. When different scattering sources exist, the contributions of the individual scattering mechanisms can be applied to analyze the observed mobility by using Matthiessen's rule [40]. To get more insight into the dominant scattering processes for oxygen-variable LBSO films, we consider lattice

phonon scattering μ_{ph}, impurity scattering μ_{imp}, and charged threading dislocations μ_{dis} as the main sources of the electron scattering. Consequently, the observed mobility in the usual approximation is

$$\mu_{\mathrm{obs}}^{-1} = \mu_{\mathrm{ph}}^{-1} + \mu_{\mathrm{imp}}^{-1} + \mu_{\mathrm{dis}}^{-1}. \tag{1}$$

The contributions derived from μ_{imp} include ionized and neutral impurities in the degenerately doped semiconductor, which are generally known as nearly temperature independent [41] and can be treated as constant. In our work, both $V_{\mathrm{O}}^{\cdot\cdot}$ and La$_{\mathrm{Ba}}^{\cdot}$ can be classified as ionized impurities. Accordingly, the major temperature-dependent processes would be ascribed to the other two scattering mechanisms. The metal-like mobility curves (oxygen pressure of 7.5 Pa) with the characteristic of higher carrier concentration have been evaluated by the following equations,

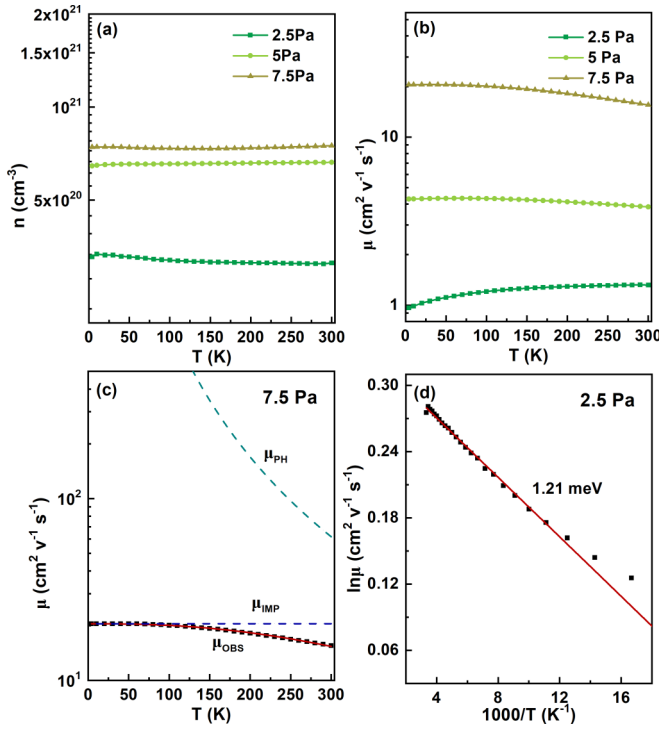$$\mu_{\mathrm{obs}}^{-1} = \mu_{\mathrm{ph}}^{-1} + \mu_{\mathrm{imp}}^{-1}, \tag{2}$$

FIG. 4. (a) Carrier concentration n and (b) mobility μ as a function of temperature at oxygen pressures of 2.5, 5, and 7.5 Pa. (c) Mobility of films grown at 7.5 Pa and contributions from different scattering mechanisms. (d) Linear fit of $\ln \mu$ vs $1000/T$ for the film grown at 2.5 Pa.

with

$$\mu_{\text{ph}} = \mu_0 \left(\frac{T}{T_0} \right)^p$$

(see Ref. [42]) and

$$\mu_{\text{imp}} = \text{const}, \tag{3}$$

where μ_0 represents the mobility at the reference temperature T_0, and p stands for the exponent of power law scaling. We attribute the temperature-independent part of the observed mobility to the μ_{imp}. The well-fitted curve provides a temperature-independent mobility μ_{imp} about 20.5 cm^2 V^{-1} s^{-1}, while an exponent p of -2.5 suggests that the scattering of carriers is mainly attributed to the acoustic phonon modes ($\lambda = -0.5$) via two-phonon processes ($\mu_{\text{ph}} \propto T^{\lambda-2}$) [43]. This demonstrates the typical competition between μ_{ph} and μ_{imp}. Due to the reduction of phonon scattering μ_{ph}^{-1} at low temperature, the mobility increases monotonously with reduced temperature. The effect of the dislocation scattering is minimal and ignorable since their charges are screened out by the high concentration of free carriers.

Though LBSO films are dominantly epilayers, additional scattering sources, such as threading dislocations (TDs) and grain boundaries, should be considered because of the large lattice mismatch with the (001) STO substrate [20]. The edge components of dislocations introduce acceptor centers along the dislocation line, and accordingly they act as acceptorlike

defects and thus capture n-type carriers from the conduction band [2,44]. A space charge layer is formed around the negatively charged dislocations to introduce extra scattering sources against electrical transport. For a lower carrier concentration under reduced oxygen pressure, the screening effect of electrons on dislocation scattering are weak, resulting in a dominant dislocation scattering μ_{dis}^{-1}. Therefore, the contributions of μ_{ph}^{-1} and μ_{imp}^{-1} are negligible. As shown in Fig. 4(d), mobilities were found to exhibit thermally activated behaviors, which suggests a dominant dislocation scattering process, in accordance with the dislocation scattering model in n-type GaN films reported previously [44], $\mu_{\text{dis}} \sim \exp(\frac{\Delta E}{kT})$, where ΔE is the electron mobility activation energy, yielding a value of 1.21 meV.

Both charged point defects ($V_{\text{O}}^{\cdot\cdot}$ and La$_{\text{Ba}}^{\cdot}$) and dislocations exist in our LBSO films. They are essential for the transport properties as observed. Based on the TEM studies as shown in Fig. S4 (see the detailed discussions in the Supplemental Material [23]), it is demonstrated that the LBSO film grown at 1 Pa has a TD density similar to the LBSO film grown at 7.5 Pa. The TD densities can be estimated approximately as $\sim 9.3 \times 10^{10}$ cm^{-2}, which is in accordance with a previous report on BaSnO$_3$/(001)SrTiO$_3$ films [45]. Accordingly, the TD density is supposed to be unchanged by merely varying the concentrations of oxygen vacancies with a fixed substrate and other growth conditions, and thereby the carrier concentration varying trend observed in our oxygen-deficient series samples is uncorrelated with the TD density. Due to the cube-on-cube relationship of LBSO film epitaxy on the STO substrate, no other grain orientations were observed (XRD phi scans displayed in Fig. S5 of the Supplemental Material [23]). On the other hand, some TDs may be arranged in the form of small angle grain boundaries. The contributions of these grain boundaries to electrical transport are similar to TDs. Unintentional native point defects may also play a non-negligible role in the evolution of electrical transports in LBSO films, if their concentrations are considerable. Therefore, intrinsic defects, including V_{O}, Sn$_i$ Bn$_i$, V_{Ba}, V_{Sn}, Sn$_{\text{Ba}}$, Ba$_{\text{Sn}}$, and O$_i$, were deliberately considered in $3 \times 3 \times 3$ Ba$_{0.963}$La$_{0.037}$SnO$_3$ supercells for studying their thermodynamic formation. Calculation results indicate that V_{O} is the most stable defect and hence plays a prominent role in the transport properties. In other words, the concentrations of other intrinsic defects are so few that they should not be responsible for the strong electron localization observed. More information on the defect thermodynamic analysis is discussed in Fig. S6 of the Supplemental Material [23]. Scanlon *et al.* have also demonstrated that the formation energy of $V_{\text{O}}^{\cdot\cdot}$ is lowest and other intrinsic defects are thermodynamically restricted in BSO under O-poor conditions by DFT [46]. As a result, we attribute the observed lower carrier concentration under decreasing growth oxygen pressure to the extra introduced oxygen vacancies, which can compensate electrons from La doping and cause strong electron localization.

Taking account of more oxygen vacancies created by the reduction of oxygen pressure, it is widely recognized that these point defects act as donorlike defects and provide two electrons simultaneously in oxides which can be written as O$_{\text{O}}^{\times} \rightarrow \frac{1}{2}O_2 + V_{\text{O}}^{\cdot\cdot} + 2e'$. In consideration of extrinsic La

donors being also expected to produce one free electron, it is reasonable to assume an increase of effective carrier concentrations with increasing oxygen vacancies. However, our work shows a result contrary to the expectations. Compared with the research of oxygen-deficient $BaSnO_3$ that has been reported, our oxygen-deficient films with heavy La impurity doping show lower carrier concentrations which may correlate with defect-defect interactions. Similar to the previous works in perovskites, experiments have evidenced that the carrier densities in oxygen-deficient $SrTiO_3$ [47] and degraded $BaTiO_3$ [48] were lower than anticipated by assuming that a single isolated oxygen vacancy provides two free electrons. It is reported that in highly reduced $SrTiO_{3-\delta}$, the oxygen vacancies tend to exist in an ordered way, such as the form of oxygen divacancies or linear clusters [49,50]. Meanwhile, they bring in deep localized states in the forbidden gap and its associated electron localization. Although defect-defect interactions, such as vacancy clustering or the interaction between the oxygen vacancy and impurity dopant, have not been previously reported in donor-doped $BaSnO_3$ thin films, it is reasonable to suppose their presence in the consideration of the thermodynamic limits to produce a uniform distribution of defects. The oxygen diffusion constant of LBSO/(001)STO films is roughly estimated to be $\sim 10^{-15}$ cm^2 s^{-1} at 530 °C [5]. This value is far lower than those of the titanates, which are on the order of 10^{-8} cm^2 s^{-1} at 600–650 °C [51].

As the deposition oxygen pressure continuously increases above 7.5 Pa, the FWHM of the rocking curves of the (002) LBSO diffractions widens. It means that the crystalline quality begins to deteriorate, accompanied by electron localization. We ascribe these worsened transport behaviors to more lattice defects, such as grain boundaries and dislocations, introduced by the poor crystalline quality at higher deposition oxygen pressures. More information on the electrical transport properties at different oxygen pressures from 7.5 to 20 Pa is shown in Fig. S7 (see the detailed discussions in the Supplemental Material [23]).

IV. BAND STRUCTURE AND DENSITY OF STATES FROM FIRST-PRINCIPLES CALCULATIONS

As the effects of other defects have been ruled out, we focus on the role of $V_O^{\cdot\cdot}$ and $La_{Ba}^{\cdot}$ on electronic structures and the consequent strong electron localization by further first-principles calculations. First, we calculated the band structure and density of states (DOS) on both undoped $BaSnO_3$ and $(Ba, La)SnO_3$ in the LDA scheme, which are consistent with the research published previously [6,52]. These calculations predict that $BaSnO_3$ has an indirect band gap and the Fermi level lies in the band gap based on the electronic band structure in Fig. 5(a). When a Ba^{2+} ion is substituted by the La^{3+} ion in the $3 \times 3 \times 3$ supercell, corresponding to the La doping rate of $x = 0.037$ in $La_xBa_{1-x}SnO_3$, the $La_{Ba}^{\cdot}$ defect acts as an electron donor and moves the Fermi level into the conduction band as shown in Fig. 5(b).

Based on the La^{3+} ion impurity doping, the evolution of the band structures of $(Ba, La)SnO_3$ with extra oxygen vacancies was further investigated. Various configurations of $(Ba, La)SnO_3$ with both single and two oxygen vacancies in a $3 \times 3 \times 3$ unit supercell are pondered. The structural
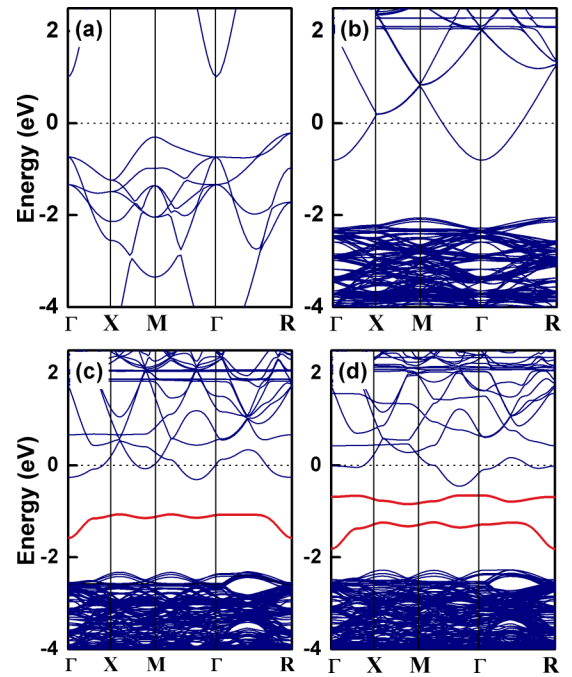

FIG. 5. The band structure of (a) $BaSnO_3$, (b) $Ba_{0.963}La_{0.037}SnO_3$, (c) $Ba_{0.963}La_{0.037}SnO_{2.988}$, and (d) $Ba_{0.963}La_{0.037}SnO_{2.975}$ from first-principles calculations with a $3 \times 3 \times 3$ supercell. For $Ba_{1-x}La_xSnO_3$, one of the Ba^{2+} ions is substituted by the La^{3+} ion equivalent to a doping rate of $x = 0.037$. Based on the La^{3+} ion impurity doping, an extra oxygen vacancy was (two extra vacancies were) introduced in a $3 \times 3 \times 3$ supercell in the form of $Ba_{0.963}La_{0.037}SnO_{2.988}$ ($Ba_{0.963}La_{0.037}SnO_{2.975}$).

configurations are displayed in Figs. S9 and S10, and consequently the ground-state energies after structural relaxation are presented in Fig. S11 of the Supplemental Material [23]. The band structures of $La_{0.037}Ba_{0.963}SnO_{2.988}$ with minimal ground-state energy are exhibited in Fig. 5(c). An additional localized state with the energy level located at 0.76 eV below the conduction minimum is observed, accompanied by the reduction of DOS near the Fermi level. This in-gap state suggests the defect-defect interactions of codoped $V_O^{\cdot\cdot}$ and $La_{Ba}^{\cdot}$ ions. For higher oxygen vacancy densities, two oxygen vacancies were created in the $3 \times 3 \times 3$ supercell. The most stable configuration with minimal ground-state energy was also chosen to be analyzed for several configurations tested. As can be seen in Fig. 5(d), another in-gap state is introduced in the forbidden gap, resulting in two separate occupied localized states. The band structure manifests that partial electrons are localized in the in-gap states.

Considering the total and partial DOS of $BaSnO_3$ systems, our results of undoped $BaSnO_3$ and $(Ba, La)SnO_3$ (shown in Fig. S8 of the Supplemental Material [23]) are quite similar to the published studies [6,36]. It is clear that the conduction band minimum (CBM) of $BaSnO_3$ mainly originates from Sn $5s$ orbitals and produces a large band dispersion, while the valence band maximum (VBM) is dominantly comprised of O $2p$ characters. By substituting the Ba^{2+} sites partly of $BaSnO_3$ with the La^{3+} ions, the Fermi level appears in the CBM which is mainly derived from the hybridization between the Sn $5s$ states and the O $2p$ states with a Sn-O antibonding
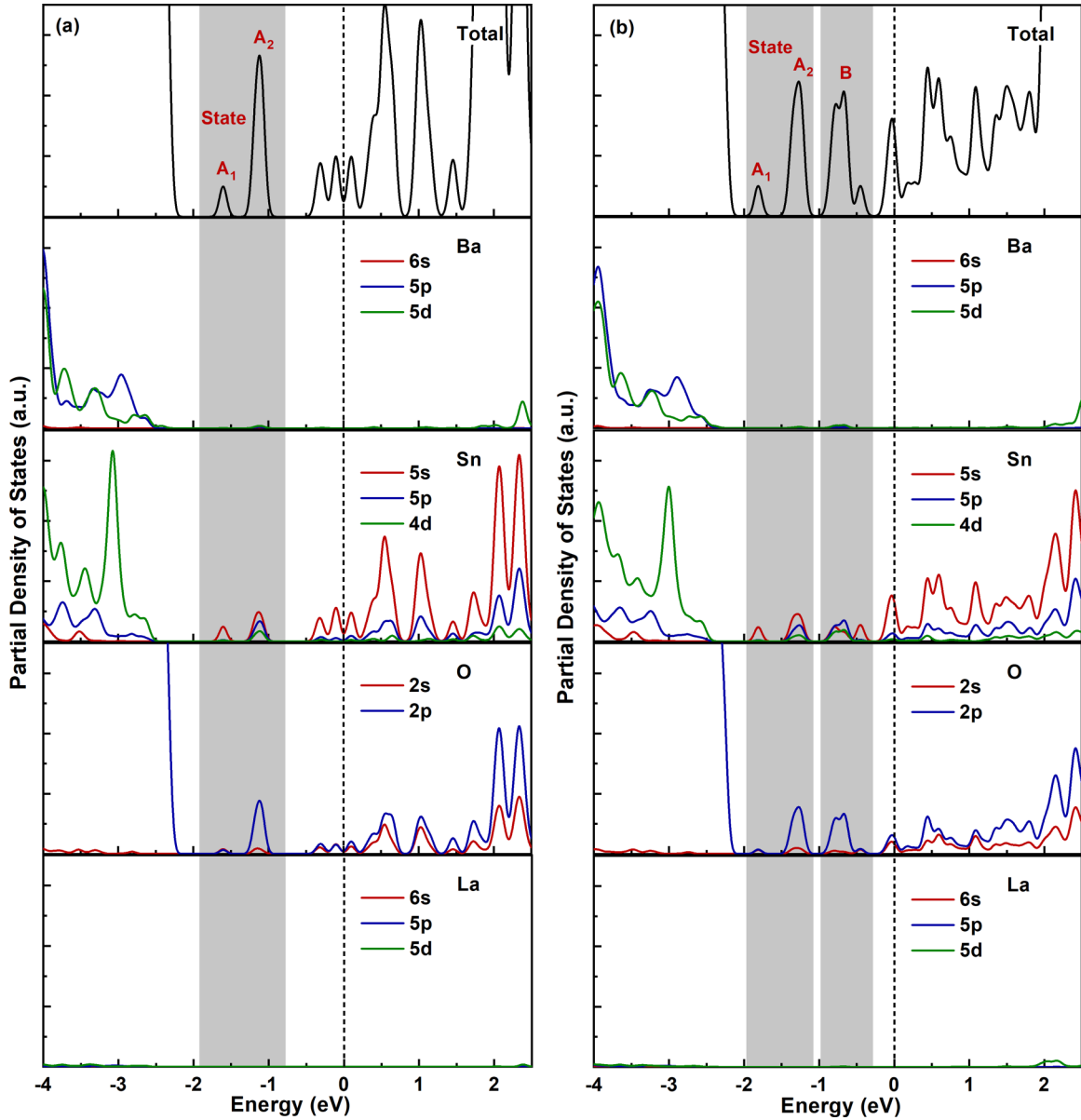
FIG. 6. Total and partial DOS of the cubic $La_{0.037}Ba_{0.963}SnO_3$ with extra (a) single oxygen vacancy and (b) two oxygen vacancies introduced.

character. However, additional DOS from in-gap states are present in the forbidden band with extra oxygen vacancies introduced. As shown in Fig. 6(a), the DOS of a single localized state [state A (A_1 and A_2)] around 0.76 eV below the CBM is composed of two parts. The lower-energy part (A_1) consists of Sn $5s$ and O $2s2p$ orbitals, and the higher-energy part (A_2) mainly corresponds to the hybridization of O $2p$ orbitals and Sn $5s5p$ with some amount of Sn $4d$ orbitals. For

the two oxygen vacancy case in Fig. 6(b), another localized state (state B) appears between state A and the CBM, which is denoted as state B. State B is composed of three parts. The two lower-energy parts are composed of Sn $5s5p4d$ and O $2s2p$ orbitals, while the higher-energy part is mainly composed of Sn $5s$ and O $2p$ orbitals.

Ba outer shell orbitals contribute no density to the DOS near the Fermi level, except the very little contribution from

TABLE II. The separate contribution of atomic orbitals for the DOS of a single oxygen vacancy introduced.

	Ba $6s$	Ba $6p$	Ba $5d$	Sn $5s$	Sn $5p$	Sn $4d$	O $2s$	O $2p$	La $6s/5p/5d$
A_1 (%)	0	0	0.47	57.24	4.91	3.74	18.46	15.19	0
A_2 (%)	0	1.09	1.99	24.39	16.28	8.30	4.43	43.53	0
Total (%)	0	0.94	1.78	28.93	14.70	7.67	6.37	39.61	0

TABLE III. The separate contribution of atomic orbitals for the DOS of two oxygen vacancies introduced.

	Ba $6s$	Ba $6p$	Ba $5d$	Sn $5s$	Sn $5p$	Sn $4d$	O $2s$	O $2p$	La $6s/5p/5d$
A_1 (%)	0	0	0.60	56.96	5.28	4.08	15.59	17.51	0
A_2 (%)	0	0.39	1.05	27.07	14.74	5.88	5.77	44.97	0.13
B (%)	0	0.94	2.80	20.70	19.08	10.88	4.84	40.31	0.41
Total (%)	0	0.65	1.93	25.67	16.39	8.36	5.91	40.80	0.27

the $5d$ orbital in the in-gap states. From the partial DOS (PDOS) plot of the La outer shell orbitals in Fig. 6, La^{3+} doping in the BSO system has a negligible contribution for the DOS near the Fermi level; only several flat bands are present with energies well above the Fermi level [as shown in the band structures in Figs. 5(b)–5(d)]. The La impurity acts as electron donors and offers free carriers to make the insulating BSO conductive. Meanwhile, the DOS near the Fermi level for oxygen-deficient models decreases when compared to $(Ba, La)SnO_3$ [refer to Fig. S8(b) of the Supplemental Material [23] and the Fermi level is fixed to zero energy]. Free electrons released from the La impurity are constrained to the neighboring O and Sn atoms in the supercell, induced by the influence of extra oxygen vacancies. Consequently, electrons are mostly localized around the in-gap states and associated electron localizations occur. These results allow a good explanation for the strong electron localization observed in our experimental facts. The separate contributions of atomic orbitals for DOS in the situation of an extra single oxygen vacancy and two oxygen vacancies introduced are shown in Tables II and III, respectively.

V. CONCLUSIONS

In this work, high-quality oxygen-deficient $La_{0.04}Ba_{0.96}SnO_3$ thin films epitaxially grown on (001) $SrTiO_3$ substrates were prepared in a wide range of oxygen pressures by PLD. The defect-defect interactions between the $V_O^{\cdot\cdot}$ and La^{3+} ions and their associated strong electron localization have been observed in both experimental results and first-principles calculations on the $BaSnO_3$ system. Based on the La^{3+} ion impurity doping, in-gap states are introduced into $(Ba, La)SnO_3$ with extra oxygen vacancies

originating from the lower growth oxygen pressures. Free electrons mainly originating from the La^{3+} donors are localized around the neighboring O and Sn atoms in the supercell with extra oxygen vacancies being introduced. Consequently, the in-gap states which are mainly derived from the combination of O $2p$ and hybridized Sn $5s5p$ with some amount of Sn $4d$ orbitals appearing in the forbidden band are revealed by first-principles calculations. Reflected on the electrical transports, an obvious transition crossing from metallic to insulating behavior occurs, followed by a decrease in both carrier concentrations and mobility in oxygen-deficient LBSO films. Considering the abundance of intrinsic and extrinsic defects in wide-gap perovskite oxide materials, it is significantly meaningful in the study of defects and related electronic states in the $BaSnO_3$ system for more scientific challenges and further insight into perovskite oxide-based devices.

[1] S. S. Shin, E. J. Yeom, W. S. Yang, S. Hur, M. G. Kim, J. Im, J. Seo, J. H. Noh, and S. I. Seok, Science **356**, 167 (2017).

[2] W.-J. Lee, H. J. Kim, J. Kang, D. H. Jang, T. H. Kim, J. H. Lee, and K. H. Kim, Annu. Rev. Mater. Res. **47**, 391 (2017).

[3] H. Mizoguchi, H. W. Eng, and P. M. Woodward, Inorg. Chem. **43**, 1667 (2004).

[4] H.-R. Liu, J.-H. Yang, H. J. Xiang, X. G. Gong, and S.-H. Wei, Appl. Phys. Lett. **102**, 112109 (2013).

[5] H. J. Kim, U. Kim, H. M. Kim, T. H. Kim, H. S. Mun, B.-G. Jeon, K. T. Hong, W.-J. Lee, C. Ju, K. H. Kim, and K. Char, Appl. Phys. Express **5**, 061102 (2012).

[6] H. J. Kim, U. Kim, T. H. Kim, J. Kim, H. M. Kim, B.-G. Jeon, W.-J. Lee, H. S. Mun, K. T. Hong, J. Yu, K. Char, and K. H. Kim, Phys. Rev. B **86**, 165205 (2012).

[7] A. Prakash, P. Xu, A. Faghaninia, S. Shukla, J. W. Ager III, C. S. Lo, and B. Jalan, Nat. Commun. **8**, 15167 (2017).

[8] Y. Tokura, *Colossal Magnetoresistive Oxides* (CRC Press, Boca Raton, FL, 2014).

[9] R. Cava, B. Batlogg, J. Krajewski, R. Farrow, L. Rupp Jr, A. White, K. Short, W. Peck, and T. Kometani, Nature (London) **332**, 814 (1988).

[10] C. Ahn, K. Rabe, and J.-M. Triscone, Science **303**, 488 (2004).

[11] T. Kimura, T. Goto, H. Shintani, K. Ishizaka, T.-h. Arima, and Y. Tokura, Nature (London) **426**, 55 (2003).

[12] I. Zeljkovic, Z. Xu, J. Wen, G. Gu, R. S. Markiewicz, and J. E. Hoffman, Science **337**, 320 (2012).

[13] A. Kalabukhov, R. Gunnarsson, J. Börjesson, E. Olsson, T. Claeson, and D. Winkler, Phys. Rev. B **75**, 121404(R) (2007).

[14] J. P. Hodges, S. Short, J. D. Jorgensen, X. Xiong, B. Dabrowski, S. M. Mini, and C. W. Kimball, J. Solid State Chem. **151**, 190 (2000).

[15] J. Kim, D. Yoon, M. Jeon, D. Kang, J. Kim, and H. Lee, Curr. Appl. Phys. **10**, 1297 (2010).

[16] N. Aristidou, C. Eames, I. Sanchez-Molina, X. Bu, J. Kosco, M. S. Islam, and S. A. Haque, Nat. Commun. **8**, 15218 (2017).

[17] Q. Liu, J. Dai, Y. Zhang, H. Li, B. Li, Z. Liu, and W. Wang, J. Alloys Compd. **655**, 389 (2016).

[18] H. M. I. Jaim, S. Lee, X. Zhang, and I. Takeuchi, Appl. Phys. Lett. **111**, 172102 (2017).

[19] D. Yoon, S. Yu, and J. Son, NPG Asia Mater. **10**, 363 (2018).

[20] W.-J. Lee, H. J. Kim, E. Sohn, H. M. Kim, T. H. Kim, K. Char, J. H. Kim, and K. H. Kim, Phys. Status Solidi A **212**, 1487 (2015).

[21] K. Ganguly, A. Prakash, B. Jalan, and C. Leighton, APL Mater. **5**, 056102 (2017).

[22] G. Kresse and J. Furthmüller, Phys. Rev. B **54**, 11169 (1996).

[23] See Supplemental Material at http://link.aps.org/supplemental/10.1103/PhysRevB.100.165312 for more XRD characterizations, other details of the transport properties, the cross-sectional TEM analyses, the defect thermodynamic analyses from first-principles calculations, and supplementary calculational information for studying strong electron localization and transmittance spectra of the LBSO/STO heterostructures, which includes Refs. [24–36].

[24] A. Prakash, P. Xu, X. Wu, G. Haugstad, X. Wang, and B. Jalan, J. Mater. Chem. C **5**, 5730 (2017).

[25] S. Chen, A. Walsh, X. G. Gong, and S. H. Wei, Adv. Mater. **25**, 1522 (2013).

[26] C. Freysoldt, J. Neugebauer, and C. G. Van de Walle, Phys. Rev. Lett. **102**, 016402 (2009).

[27] C. Persson, Y.-J. Zhao, S. Lany, and A. Zunger, Phys. Rev. B **72**, 035211 (2005).

[28] P. Xu, S. Chen, H.-J. Xiang, X.-G. Gong, and S.-H. Wei, Chem. Mater. **26**, 6068 (2014).

[29] S. Dabaghmanesh, R. Saniz, M. N. Amini, D. Lamoen, and B. Partoens, J. Phys.: Condens. Matter **25**, 415503 (2013).

[30] S. Sallis, D. O. Scanlon, S. C. Chae, N. F. Quackenbush, D. A. Fischer, J. C. Woicik, J. H. Guo, S. W. Cheong, and L. F. J. Piper, Appl. Phys. Lett. **103**, 042105 (2013).

[31] Z. Lebens-Higgins, D. O. Scanlon, H. Paik, S. Sallis, Y. Nie, M. Uchida, N. F. Quackenbush, M. J. Wahila, G. E. Sterbinsky, D. A. Arena, J. C. Woicik, D. G. Schlom, and L. F. J. Piper, Phys. Rev. Lett. **116**, 027602 (2016).

[32] J. Tauc, R. Grigorovici, and A. Vancu, Phys. Status Solidi B **15**, 627 (1966).

[33] Q. Liu, J. Dai, Z. Liu, X. Zhang, G. Zhu, and G. Ding, J. Phys. D: Appl. Phys. **43**, 455401 (2010).

[34] H. F. Wang, Q. Z. Liu, F. Chen, G. Y. Gao, W. Wu, and X. H. Chen, J. Appl. Phys. **101**, 106105 (2007).

[35] B. Li, Q. Liu, Y. Zhang, Z. Liu, and L. Geng, J. Alloys Compd. **680**, 343 (2016).

[36] J. B. Pendry, A. J. Holden, W. J. Stewart, and I. Youngs, Phys. Rev. Lett. **76**, 4773 (1996).

[37] D. Y. Yoo, E. Chong, D. H. Kim, B. K. Ju, and S. Y. Lee, Thin Solid Films **520**, 3783 (2012).

[38] E. Abrahams, P. W. Anderson, D. C. Licciardello, and T. V. Ramakrishnan, Phys. Rev. Lett. **42**, 673 (1979).

[39] Q. Liu, J. Liu, B. Li, H. Li, G. Zhu, K. Dai, Z. Liu, P. Zhang, and J. Dai, Appl. Phys. Lett. **101**, 241901 (2012).

[40] J. M. Ziman, *Electrons and Phonons: The Theory of Transport Phenomena in Solids* (Oxford University Press, Oxford, UK, 2001).

[41] D. Chattopadhyay and H. J. Queisser, Rev. Mod. Phys. **53**, 745 (1981).

[42] S. Kasap and P. Capper, *Springer Handbook of Electronic and Photonic Materials* (Springer, Berlin, 2017).

[43] E. Gershtein, T. Stavitskaia, and L. Stilbans, Sov. Phys. Tech. Phys. **2**, 2302 (1957).

[44] H. M. Ng, D. Doppalapudi, T. D. Moustakas, N. G. Weimann, and L. F. Eastman, Appl. Phys. Lett. **73**, 821 (1998).

[45] H. Mun, U. Kim, H. M. Kim, C. Park, T. H. Kim, H. J. Kim, K. H. Kim, and K. Char, Appl. Phys. Lett. **102**, 252105 (2013).

[46] D. O. Scanlon, Phys. Rev. B **87**, 161201(R) (2013).

[47] W. Gong, H. Yun, Y. Ning, J. Greedan, W. Datars, and C. Stager, J. Solid State Chem. **90**, 320 (1991).

[48] D. I. Woodward, I. M. Reaney, G. Y. Yang, E. C. Dickey, and C. A. Randall, Appl. Phys. Lett. **84**, 4650 (2004).

[49] P. Lodahl, A. Floris Van Driel, I. S. Nikolaev, A. Irman, K. Overgaag, D. Vanmaekelbergh, and W. L. Vos, Nature (London) **430**, 654 (2004).

[50] K. Eom, E. Choi, M. Choi, S. Han, H. Zhou, and J. Lee, J. Phys. Chem. Lett. **8**, 3500 (2017).

[51] J. Maier, G. Schwitzgebel, and H.-J. Hagemann, J. Solid State Chem. **58**, 1 (1985).

[52] Y. Kang, H. Peelaers, K. Krishnaswamy, and C. G. Van de Walle, Appl. Phys. Lett. **112**, 062106 (2018).